A Pairwise Distance Distribution Correction (DDC) algorithm for blinking-free super-resolution microscopy

Christopher H. Bohrer[1, 3], Xinxing Yang[1], Xiaoli Weng[1], Brian Tenner[2], Brian Ross[2], Ryan Mcquillen[1], Jin Zhang[2], Elijah Roberts[3], and Jie Xiao[1]

[1] Department of Biophysics and Biophysical Chemistry, Johns Hopkins School of Medicine
[2] Department of Pharmacology, University of California, San Diego
[3] Department of Biophysics, Johns Hopkins University

Abstract

In single-molecule localization based super-resolution microscopy (SMLM), a fluorophore stochastically switches between fluorescent- and dark-states, leading to intermittent emission of fluorescence. Intermittent emissions create multiple localizations belonging to the same molecule, a phenomenon known as blinking. Blinking distorts SMLM images and confound quantitative interpretations by forming artificial nanoclusters, which are often interpreted as true biological assemblies. Multiple methods have been developed to eliminate these artifacts, but they either require additional experiments, arbitrary thresholds, or specific photo-kinetic models. Here we present a method, termed Distance Distribution Correction (DDC), to eliminate fluorophore blinking in superresolution imaging without any additional calibrations. The approach relies on the finding that the true pairwise distance distribution of different fluorophores in an SMLM image can be naturally obtained from the imaging sequence by using the distances between localizations separated by a time much longer than the average fluorescence survival time. We show that using the true pairwise distribution we can define and then maximize the likelihood of obtaining a particular set of localizations without blinking and generate an accurate reconstruction of the true underlying cellular structure. Using both simulated and experimental data, we show that DDC surpasses all previous existing blinking correction methodologies, resulting in drastic improvements in obtaining the closest estimate of the true spatial organization and number of fluorescent emitters. The simplicity and robustness of DDC will enable its wide application in SMLM imaging, providing the most accurate reconstruction and quantification of SMLM images to date.

Introduction

In recent years the development of superresolution fluorescence microscopy has enabled the probing of macromolecular assemblies in cells with nanometer resolutions. Amongst different superresolution imaging techniques, single-molecule localization superresolution microscopy (SMLM) has gained wide popularity due to its relatively simple implementation, which is based on post-imaging analysis of single-molecule detection.

SMLM reconstructs a superresolution image by stochastic photo-activation of individual fluorophores and subsequent accurate post-imaging localization determination (1–3). One major advantage of SMLM is that due to its single-molecule detection nature, one can determine the number of molecules in a macromolecular assembly quantitatively, allowing the investigation of both the molecular composition and spatial arrangement at a level unmatched by other ensemble imaging-based superresolution imaging techniques. In the past few years SMLM has led to novel discoveries and quantitative characterizations of numerous biological assemblies (4, 5) such as those composed of RNA polymerase (6–8), membrane proteins (9), bacterial divisome proteins (10–13), synaptic proteins (14, 15), the cytoskeleton (16), DNA binding proteins (17, 18), chromosomal DNA (19), viral proteins (20), and more.

One critical aspect in realizing the full quantitative potential of SMLM relies on the careful handling of the blinking behavior of fluorophores. A photo-switchable fluorophore can switch multiple times between activated and dark states before it is permanently photobleached, leading to repeated localizations from the same molecule. These repeated localizations are often mis-identified as multiple molecules, resulting in the appearance of false nanoclusters and counting errors in the number of molecules and stoichiometry of complexes (Fig. 1A) (21–25).

Multiple groups have developed different methods to correct for blinking effects in SMLM. These methods can be coarsely divided into two categories depending on whether a method provides a blinking-corrected image at the single molecule level or a statistical analysis summarizing the properties of the image at the ensemble level. Methods in the first category commonly use a variety of threshold values both in time and space to group localizations that likely come from the same molecule (1, 2, 21, 23, 25, 26). The advantage of using thresholds is that it results in a blinking-corrected image, allowing one to observe the spatial distribution of fluorophores in cells and apply other quantitative analyses as needed. The disadvantage is that a constant threshold value is often insufficient in capturing the stochastic nature of fluorophore blinking and heterogeneous molecular assemblies. Furthermore, calibration experiments and/or a priori knowledge of the fluorophore's photochemical properties are often needed to determine the appropriate threshold values (21, 23, 25, 27, 28). Statistical analyses such as maximum likelihood or Bayesian approaches have been developed to take into account the stochastic behavior of blinking to count the number of fluorophores, but have yet to produce a blinking-corrected superresolution image (29–31). Additionally, many of these approaches are dependent on specific photokinetic models for the fluorophore, which can be complex and difficult to determine (27, 28, 32–35).

The second category of methods analyze raw, uncorrected SMLM images using statistical methods to characterize the mean properties of the organization of molecules at the ensemble level. Pair- or auto-correlation-based analyses (PCA) have been used extensively within the field (24, 36). The long tail of the correlation function can often be fit to a specific model to extract quantitative parameters. This class of methods is prone to model-specific errors, especially if the underlying structures of the molecular assemblies are heterogeneous and vary throughout the image (37). A recently developed method analyzes the clustering of a protein with experimentally varied labeling densities, which was robust in determining whether membrane proteins form nanoclusters and was insensitive to many imaging artifacts (22). A post-imaging computational analysis capitalizing on the same principle has also been developed (38). Although these

77 methods are powerful in determining whether a protein of interest forms clusters or not, they provide a
78 quantification at the ensemble level but not a blinking-corrected image, which limits their use in analyzing
79 heterogeneously distributed molecular assemblies and their spatial arrangement in cells.

81 Here, we present an algorithm, termed Distance Distribution Correction (DDC), to enable robust recon-
82 struction and quantification of blinking-free SMLM superresolution images without the need of setting
83 empirical thresholds or performing experiments to calibrate a fluorophore's blinking kinetics. We first
84 validate our approach using a diverse set of simulated and experimental data and compare DDC to other
85 existing methods. In each situation DDC outperformed the existing methods in obtaining the closest rep-
86 resentation of the underlying blinking-free image and in determining the accurate number of fluorophores.
87 We also applied DDC to experimentally collected SMLM images of two orthologs of a scaffolding protein
88 that is important for the organization of membrane microdomains, A-Kinase Anchoring Protein 79/150
89 (AKAP79 and AKAP150) (39, 45, 46). Both proteins showed clustered organizations, but with signifi-
90 cantly reduced numbers and sizes of clusters when compared to the commonly used thresholding method,
91 changing the quantitative properties of membrane microdomains organized by these proteins. Finally, we
92 discuss critical considerations of how to apply DDC to experiments successfully.

Results

Principle of DDC

96 DDC is based on the principle that the pairwise distance (Δr) distribution, $P_d(\Delta r|\Delta n)$, of the localiza-
97 tions separated by a frame difference (Δn) much larger than the average number of frames a molecule's
98 fluorescence lasts (N) approximates the true pairwise distance distribution $P_T(\Delta r)$. Note that N does
99 not need to be precisely determined as long as it is in the regime where $P_d(\Delta r|\Delta n)$ approaches a steady
100 state, as we show below. One intuitive way to understand this principle is that, if one collects an imaging
101 stream that is long enough so that all the localizations in the first and last frames of the stream come
102 from distinct sets of fluorophores, the pairwise distance distribution between the localizations of the two
103 frames will then be devoid of blinking and will reflect the true pairwise distance distribution ($P_T(\Delta r)$).
104 A mathematical justification of this principle is provided in the supplemental material with an in-depth
105 discussion and illustration (Fig. S1).

107 To demonstrate the principle of DDC, we used simulated SMLM images of randomly distributed fluo-
108 rophores that followed the photokinetic model shown in Fig. S2A. One representative superresolution
109 image and the corresponding scatter plot, colored through time, with and without blinking are shown in
110 Fig. 1A. Apparent clustering was observed in images when blinking was not corrected. Using the un-
111 corrected images, we computed the pairwise distance distributions at all frame differences Δn (Fig. 1B).
112 As shown in Fig. 1C and Fig. S3, at small Δn there are large peaks at short distances, indicating that
113 there were repeated localizations from the same fluorophores closely spaced in time and space. When Δn
114 is large, the pairwise distance distributions approach a steady state converging upon the true pairwise
115 distance distribution (Fig. 1C, dotted curve). This behavior supports the principle that when Δn is large
116 the pairwise distance distribution represents the true pairwise distance distribution. Using simulations,
117 we also show that the pairwise distance distributions converge upon the true distributions at large Δn ir-
118 respective of the underlying photokinetics or molecular spatial distributions (Fig. S3, Supporting Material).

120 Next, we used experimentally obtained SMLM images of three molecular assemblies labeled with dif-
121 ferent fluorophores in *E. coli* cells, the bacterial transcription elongation factor NusA fused with the
122 reversibly switching green fluorescent protein Dronpa (40), *E. coli* RNA Polymerase fused with the

photoactivatable red fluorescent protein PAmCherry (41), and precursor ribosomal RNAs (pre-rRNA) labeled with organic fluorophore Alexa647-conjugated DNA probes (42) (Fig. S4, Supporting Material). We determined the pairwise distance distribution for each fluorophore and calculated the normalized, summed differences of the cumulative distributions for each Δn, relative to that of $\Delta n = 1$, $(Z(\Delta n) = \sum |cdf(P_d(\Delta r|\Delta n)) - cdf(P_d(\Delta r|\Delta n = 1))|)$. As shown in Fig. 1D, in all cases the corresponding normalized Z reach plateaus at large Δn despite different photokinetics and spatial distributions. The rate at which each fluorophore reaches the plateau for the normalized Z reflects the photokinetics of the fluorophore; the longer a fluorophore blinked (such as Alexa647 compared to Dronpa), the longer the time until Z plateaued. These experimental results further verify the principle of DDC by showing that the pairwise distance distributions converge upon a steady state distribution as Δn increases.

It is important to note that the determination of $P_T(\Delta r)$ is not dependent upon a particular photokinetic model of the fluorophore nor does it require experimental characterizations of the fluorophore. $P_T(\Delta r)$ can be determined solely from the SMLM image stream as long as it is long enough so that a steady state of $P_d(\Delta r|\Delta n)$ can be reached (Fig. 1C, Fig. S3).

Once determined, $P_T(\Delta r)$ can then be used to calculate the likelihood to have a particular subset of true localizations (Fig. S5-S9, Supporting Material) using the following equation:

$$\mathcal{L}(\{B,T\}|\mathbf{r},\mathbf{n}) = \prod_{i,j\in\{T\}} P_T(\Delta r_{i,j}) \times \prod_{i\in\{B\},j\in\{B,T\}} P_{B1}(\Delta r_{i,j}|\Delta n_{i,j}), \tag{1}$$

where $\{B,T\}$ are sets that contain the indices of the localizations that are considered blinks $\{B\}$ and the true localizations $\{T\}$ given the coordinates $\mathbf{r}$ and associated frame numbers $\mathbf{n}$ obtained from experiment. The first term on the right of the equation is the probability of observing all distances Δr between every pair of true localizations (i & $j \in \{T\}$). Here the probability distribution $P_T(\Delta r_{i,j})$ is the true pairwise distance distribution. The second term is the probability of observing all distances between pairs of localizations with at least one being a blink ($i \in \{B\}$ and $j \in \{B,T\}$). Here, the probability distribution $P_{B1}(\Delta r_{i,j}|\Delta n_{i,j})$ gives the probability of observing a distance between a pair of localizations with a frame difference $\Delta n_{i,j}$ if at least one of the localizations is a blink. This probability distribution can be easily determined once $P_T(\Delta r)$ is known (Supporting Material). Here, maximizing the likelihood with respect to $\{B,T\}$ results in a subset of true localizations where the pairwise distance distributions $P_d(\Delta r|\Delta n)$ are equal to $P_T(\Delta r)$ (Fig. S6). DDC maximizes the likelihood with respect to the two sets ({B, T}) using a Markov Chain Monte Carlo (MCMC) (43, 44), to result in the blinking corrected image (Fig. S8 and S9, Supporting Material).

To validate Equation 1, we show that only when greater than 97% of the final localizations are the true localizations does the likelihood reach its maximum (Fig. S7). This result was observed regardless of distinct spatial distribution or photo-kinetics of the fluorophore in six different simulations (Fig. S7).

DDC outperforms existing methods in both image reconstruction and counting the number of molecules

To compare the performance of DDC with commonly used thresholding methods, we simulated four systems, random distribution (no clustering), small clusters, dense clusters, and filamentous structures (Fig. 2, Supporting Material). In these simulations the fluorophore had two dark states and followed the photokinetic model shown in Fig. S2A. The raw images without any blinking-correction for each simulation are shown in Fig. 2A. We applied DDC, three published thresholding methods (T1 to T3 (21, 23, 25))(Supporting Material, Fig. S10 and S11) and a customized thresholding method (T4, Sup-

porting Material) to all the images. Method T1 links together localizations using a time threshold that is determined using an empirical estimation of the photokinetics of the fluorophore (21) (Fig. S10, Supporting Material). Method T2 uses the experimentally quantified photo-kinetics of the fluorophore to set extreme thresholds so that the possibility of overcounting is extremely low (25). Method T3 uses the experimentally determined number of blinks per fluorophore to choose thresholds that result in the correct number of localizations within each image (23)(Fig. S11, Supporting Material). T2 and T3, but not T1, require additional experiments to characterize fluorophore photo properties. Method T4 is a customized, ideal thresholding method that scans all possible thresholds and uses the thresholds that result in the least Image Error for each system (Supporting Material). T4 cannot be applied in real experiments since the true, blink-free image is unknown, and we included it here to illustrate the best scenario of what a thresholding method could achieve. To quantitatively compare the ability of these methods in producing a blinking-corrected image we calculated two metrics, the Image Error and Counting Error (Fig. 2B, Supporting Material). The Image Error was calculated by first summing the squared difference of each pixel's normalized intensity between the blinking-corrected images and the true image, and then dividing this squared difference by the error between the uncorrected image and the true image (Supporting Material). The Image Error quantifies the amount of error in determining the distribution of localizations without being penalized for the error in the number of localizations. The Counting Error was calculated as the difference between the true number of fluorophores and that determined from the blinking-corrected image divided by the actual number of fluorophores (Supporting Material).

As shown in Fig. 2B, DDC outperforms all four methods by having the lowest Image Errors and lowest (or close-to-lowest) Counting Errors. Interestingly, even with the best possible thresholds (T4), DDC still outperforms T4 in determining the correct spatial distribution and numbers of localizations. This result suggests that thresholds cannot adequately account for the stochastic nature of blinking. Similar results are shown in Fig. S12 for a fluorophore with one dark state (Fig. S2B). When counting the number of localizations is the main concern, T3 performs equally or slightly better than DDC because T3 was applied with an experimental calibration that provides the average number of blinks per fluorophore (Fig. 2, Supporting Material). Nonetheless, DDC outperforms T3 by having lower Image Errors across all four different simulation systems, especially for the dense cluster system, where the average Image Error of T3 is seven times that of DDC (Fig. 2B). In conclusion, these results indicate that DDC can be used to obtain the correct number of true localizations and at the same time produce the most accurate SMLM images.

DDC identifies differential clustering properties of membrane microdomain proteins AKAP79 and AKAP150

Membrane microdomains formed by membrane proteins have been commonly observed in super-resolution imaging studies and have raised significant interest in their molecular compositions and associated biological functions (9). However, concerns remain as of whether the characterizations of these microdomain protein clusters were impacted by blinking (22). Here we used DDC to investigate a membrane scaffolding protein, A-Kinase Anchoring Protein (AKAP), which plays an important role in the formation of membrane microdomains (39, 45, 46). The two orthologs AKAP79 (human) and AKAP150 (rodent) were previously shown to form dense membrane clusters, which are likely important for regulating anchored kinase signaling.

We performed SMLM imaging on AKAP150 in murine pancreatic beta cells using an anti-AKAP150 antibody and analyzed the resulting SMLM data using DDC (Supporting Material). For AKAP79, we applied DDC to previously acquired SMLM data from HeLa cells (39). For comparison, we also applied the T1 method to both scaffolding proteins as it was used in the previous study of the AKAP79 (21, 39) (Fig.

S13, S14). We found that the images from DDC still showed significant deviations from what was expected from simulated random distributions, indicating the presence of clustering. We also observed that DDC images exhibited dramatically reduced clustering when compared to the uncorrected and T1-corrected images for both proteins (Fig. 3A). To quantitatively compare these images, we used a tree-clustering algorithm (Supporting Material) to group localizations in individual clusters and show the corresponding cumulative distributions in Fig. 3B. The cumulative distributions show that the degrees of clustering for both proteins are significantly reduced when DDC was applied. Interestingly, AKAP150 shows a higher degree of clustering when compared to AKAP79, with more than 50% of the localizations within clusters containing greater than 15 localizations, twice that of AKAP79. Nevertheless, DDC-corrected AKAP79/150 images show significant deviations from the simulated random distributions, indicating the presence of clustering (Fig. 3B, compare yellow and purple curves). These results suggest that the clustering of the AKAP scaffolds are differentially regulated and the context dependence is likely important in considering the microdomain-specific signaling functions of the clusters.

Considerations in the application of DDC

As with any method, successful application of DDC to SMLM images requires an understanding of critical factors that could influence the performance of DDC. In this section, we evaluate the impact of localization density and activation rate on the performance of DDC using simulations. We also demonstrate that the commonly used practice of ramping the UV activation power in SMLM imaging should be avoided when applying DDC.

To quantify the influence of localization density on the performance of DDC, we simulated random distributions of fluorophores with different densities ranging from 1000 raw localizations to 15000 localizations per $1\mu m^2$. Note that a density greater than 5000 localizations/μm^2 corresponds to a Nyquist resolution of 30 nm or better. As shown in Fig. 4A, the Image Error increases as the localization density increases and reaches a plateau at $\sim .35$. We found that the increase in Image Error at high localization densities was mostly due to the decreased raw Image Error of the uncorrected images at high localization densities (Fig. S15A). The decreasing improvement of DDC at increasing sampling rate suggests that a high sampling rate of the underlying structure reduces the image distortion caused by blinking, although very high labeling densities ($> 10,000$ localizations/μm^2) is usually difficult to achieve for protein assemblies.

Next, to quantify the influence of the activation rate, we varied the activation probability of each simulated fluorophore from .025 to .15 per frame, with 1000 fluorophores randomly distributed throughout a $1\mu m^2$ area. Fig. 4B shows that the Image Error of DDC steadily increases with the activation rate. This increase was because at high activation rates, the temporal overlaps of individual fluorophores that were spatially close to each other increased, which made it difficult to distinguish blinks from different fluorophores. Thus, as with all the other blinking methodologies, DDC obtains the best images when the activation rate is slow.

Finally, we illustrate one critical requirement for the successful application of DDC, that is, the photokinetics (blinking behavior) of the fluorophore, must be kept constant throughout the acquisition of the SMLM imaging stream (Supporting Material). Note that this requirement is also needed for all other blinking correction methods (21, 23, 25). One common practice in SMLM imaging is to ramp the activation power gradually throughout the SMLM imaging sequence in order to speed up the acquisition at later times when the number of fluorophores in the view field gradually deplete. The assumption is that activation power only changes the activation rate of a fluorophore (i.e. the probability of a fluorophore being activated per frame), but not the photokinetics of its blinking behavior (i.e. number of blinks, dark time and fluorescence-on time). Such a scenario indeed was shown for the photoactivatable fluorescent protein Dendra (28), but there are also reports showing that the photokinetics of mEos2 and PAmCherry are sensitive to the activation intensity (27, 28).

6

We further investigated the activation dependence of the blinking behaviors of two commonly used fluorophores for SMLM imaging, the photoactivatable fluorescent protein mEos3.2 and the organic fluorophore Alexa647 with different activation (405nm) intensities. We quantified three parameters, number of blinks, off-times (T_{off}) and on-times (T_{on}), and report the mean value for each parameter as a function of activation intensity (Fig. 4C and Fig. S16.) We define one blink event as one continuous emission event that could span multiple fluorescence on-frames, the number of blinks as the number of repeated emissions separated by dark frames from the same fluorophore, T_{off} as the time between each blink and T_{on} as the time that the fluorophore remained fluorescent at each blink-on event (Fig. 4C). We observed that both fluorophores had a similar dependence of T_{on} with UV intensity, where T_{on} initially increased and then decreased at higher UV intensities (Fig. 4D, top), suggesting that UV also participates in the fluorescence emission cycle of the fluorophores. Next, we found that T_{off} decreased non-linearly as the UV intensity increased for both fluorophores (Fig. 4D, middle). Finally, we observed that the average number of blinks for the Alexa647 molecule increased dramatically with UV intensity while that of mEos3.2 remained largely constant (Fig. 4D, bottom), suggesting a differential influence of UV in changing the photokinetics of different fluorophores. Thus, varying the activation intensity during the acquisition of a SMLM image can indeed change the blinking characteristics of the fluorophores, which would affect the performance of DDC. These results suggest that changing the activation intensity should only be done when a quantitative approach is not needed, or the proper controls have been performed to show that the fluorophore is insensitive to variations in the activation intensity.

Discussion

In this work we provided a blinking-correction methodology, DDC, that does not depend upon exact thresholds, additional experiments, or a specific photo-kinetic model of the fluorophore to obtain an accurate reconstruction and quantification of SMLM superresolution images. DDC works by determining a "ground truth" about the underlying organization of fluorophores, the true pairwise distance distribution. We verified by simulations and experiments that such a true pairwise distance distribution can be obtained by taking the distances between localizations that are separated by a frame difference much longer than the average lifetime of the fluorophore. Using the true pairwise distribution, the likelihood can be calculated, where upon maximization of the likelihood one obtains an accurate representation of the true underlying structure.

We compared the performance of DDC with four different thresholding methods using simulated data with various spatial distributions and on fluorophores with different photokinetic models. DDC outperformed these methods by providing the "best" blinking-corrected images as well as excellent estimates of the number of molecules in each image.

We also used DDC to investigate the spatial organizations of two scaffolding proteins AKAP79 and AKAP150, which have been shown to form microdomain-like structures (39, 46). DDC resulted in significantly less degrees of clustering for the two proteins when compared to that resulted from the thresholding method. Most interestingly, DDC's ability to count the number of true localizations in SMLM images allowed quantitative comparison between the clusters formed by the two proteins: AKAP150 was about 2-fold more clustered than AKAP79. Such a difference in clustering could indicate that the two proteins are differentially regulated in separate cell types and this context dependence could be important for the signaling functions of the clusters. Further experiments are required to explore these possibilities. An additional note is that DDC only counts the number of emitters, which does not necessarily equal to the number of molecules that are labeled using dye-conjugated antibodies (47).

Finally, we demonstrated that the higher the activation rate and the density of fluorophores, the smaller the relative improvement of DDC. We also showed that in order to use DDC, the common practice of ramping the UV should be avoided in certain cases (depending upon the particular fluorophore), as we verified that mEos3.2 and Alexa647 exhibited activation power-dependent photokinetics. In essence, DDC is best suited for SMLM imaging when quantitative characterizations of heterogenous cellular structures are required. The complete package of DDC is available for download at https://github.com/XiaoLabJHU/DDC.

References

[1] Betzig, E., G. H. Patterson, R. Sougrat, O. W. Lindwasser, S. Olenych, J. S. Bonifacino, M. W. Davidson, J. Lippincott-Schwartz, and H. F. Hess, 2006. Imaging intracellular fluorescent proteins at nanometer resolution. Science 313:1642–1645.

[2] Rust, M. J., M. Bates, and X. Zhuang, 2006. Sub-diffraction-limit imaging by stochastic optical reconstruction microscopy (STORM). Nature Methods 3:793–796.

[3] Hess, S. T., T. P. K. Girirajan, and M. D. Mason, 2006. Ultra-high resolution imaging by fluorescence photoactivation localization microscopy. Biophysj 91:4258–4272.

[4] Baddeley, D. and J. Bewersdorf, 2018. Biological Insight from Super-Resolution Microscopy: What We Can Learn from Localization-Based Images. Annual review of biochemistry 87:965–989.

[5] Sauer, M. and M. Heilemann, 2017. Single-Molecule Localization Microscopy in Eukaryotes. Chemical Reviews 117:7478–7509.

[6] Endesfelder, U., K. Finan, S. J. Holden, P. R. Cook, A. N. Kapanidis, and M. Heilemann, 2013. Multiscale Spatial Organization of RNA Polymerase in Escherichia coli. Biophysj 105:172–181.

[7] Chen, X., M. Wei, M. M. Zheng, J. Zhao, H. Hao, L. Chang, P. Xi, and Y. Sun, 2016. Study of RNA Polymerase II Clustering inside Live-Cell Nuclei Using Bayesian Nanoscopy. ACS Nano 10:2447–2454.

[8] Weng, X. and J. Xiao, 2014. Spatial organization of transcription in bacterial cells. Trends in genetics 30:287–297.

[9] Garcia-Parajo, M. F., A. Cambi, J. A. Torreno-Pina, N. Thompson, and K. Jacobson, 2014. Nanoclustering as a dominant feature of plasma membrane organization. J Cell Sci 127:4995–5005.

[10] Coltharp, C., J. Buss, T. M. Plumer, and J. Xiao, 2016. Defining the rate-limiting processes of bacterial cytokinesis. Proceedings of the National Academy of Sciences 113:E1044–E1053.

[11] Buss, J., C. Coltharp, T. Huang, C. Pohlmeyer, S.-C. Wang, C. Hatem, and J. Xiao, 2013. In vivoorganization of the FtsZ-ring by ZapA and ZapB revealed by quantitative super-resolution microscopy. Molecular microbiology 89:1099–1120.

[12] Buss, J., C. Coltharp, G. Shtengel, X. Yang, H. Hess, and J. Xiao, 2015. A multi-layered protein network stabilizes the Escherichia coli FtsZ-ring and modulates constriction dynamics. PLoS genetics 11:e1005128.

[13] Fu, G., T. Huang, J. Buss, C. Coltharp, Z. Hensel, and J. Xiao, 2010. In vivo structure of the E. coli FtsZ-ring revealed by photoactivated localization microscopy (PALM). PLoS ONE 5:e12682.

[14] Spühler, I. A., G. M. Conley, F. Scheffold, and S. G. Sprecher, 2016. Super Resolution Imaging of Genetically Labeled Synapses in Drosophila Brain Tissue. Frontiers in cellular neuroscience 10:142.

[15] Bar-On, D., S. Wolter, S. van de Linde, M. Heilemann, G. Nudelman, E. Nachliel, M. Gutman, M. Sauer, and U. Ashery, 2012. Super-resolution imaging reveals the internal architecture of nano-sized syntaxin clusters. Journal of Biological Chemistry 287:27158–27167.

[16] Xu, K., G. Zhong, and X. Zhuang, 2013. Actin, spectrin, and associated proteins form a periodic cytoskeletal structure in axons. Science 339:452–456.

[17] Wang, W., G.-W. Li, C. Chen, X. S. Xie, and X. Zhuang, 2011. Chromosome organization by a nucleoid-associated protein in live bacteria. Science 333:1445–1449.

[18] Xie, X., M. P. Cosma, and M. Lakadamyali, 2017. ScienceDirect Super resolution imaging of chromatin in pluripotency, differentiation, and reprogramming. Current opinion in genetics & development 46:186–193.

[19] Spahn, C., U. Endesfelder, and M. Heilemann, 2014. Super-resolution imaging of Escherichia coli nucleoids reveals highly structured and asymmetric segregation during fast growth. Journal of structural biology 185:243–249.

[20] Lehmann, M., S. Rocha, B. Mangeat, F. Blanchet, H. Uji-I, J. Hofkens, and V. Piguet, 2011. Quantitative multicolor super-resolution microscopy reveals tetherin HIV-1 interaction. PLoS pathogens 7:e1002456.

[21] Annibale, P., M. Scarselli, A. Kodiyan, and A. Radenovic, 2010. Photoactivatable Fluorescent Protein mEos2 Displays Repeated Photoactivation after a Long-Lived Dark State in the Red Photoconverted Form. The Journal of Physical Chemistry Letters 1:1506–1510.

[22] Baumgart, F., A. M. Arnold, K. Leskovar, K. Staszek, M. Fölser, J. Weghuber, H. Stockinger, and G. J. Schütz, 2016. Varying label density allows artifact-free analysis of membrane-protein nanoclusters. Nature Methods 13:661–664.

[23] Coltharp, C., R. P. Kessler, and J. Xiao, 2012. Accurate Construction of Photoactivated Localization Microscopy (PALM) Images for Quantitative Measurements. PLoS ONE 7:e51725–16.

[24] Sengupta, P., T. Jovanovic-Talisman, D. Skoko, M. Renz, S. L. Veatch, and J. Lippincott-Schwartz, 2011. Probing protein heterogeneity in the plasma membrane using PALM and pair correlation analysis. Nature Methods 8:969–975.

[25] Puchner, E. M., J. M. Walter, R. Kasper, B. Huang, and W. A. Lim, 2013. Counting molecules in single organelles with superresolution microscopy allows tracking of the endosome maturation trajectory. Proceedings of the National Academy of Sciences of the United States of America 110:16015–16020.

[26] Annibale, P., S. Vanni, M. Scarselli, U. Rothlisberger, and A. Radenovic, 2011. Identification of clustering artifacts in photoactivated localization microscopy. Nature Publishing Group 8:527–528.

[27] Hartwich, T. M. P., F. V. Subach, L. Cooley, V. V. Verkhusha, and J. Bewersdorf, 2013. Determination of two-photon photoactivation rates of fluorescent proteins. Physical chemistry chemical physics : PCCP 15:14868–14872.

[28] Lee, S.-H., J. Y. Shin, A. Lee, and C. Bustamante, 2012. Counting single photoactivatable fluorescent molecules by photoactivated localization microscopy (PALM). Proceedings of the National Academy of Sciences of the United States of America 109:17436–17441.

[29] Rollins, G. C., J. Y. Shin, C. Bustamante, and S. Pressé, 2015. Stochastic approach to the molecular counting problem in superresolution microscopy. Proceedings of the National Academy of Sciences of the United States of America 112:E110–8.

[30] Hummer, G., F. Fricke, and M. Heilemann, 2016. Model-independent counting of molecules in single-molecule localization microscopy. Molecular biology of the cell 27:3637–3644.

[31] Nino, D., N. Rafiei, Y. Wang, A. Zilman, and J. N. Milstein, 2017. Molecular Counting with Localization Microscopy: A Bayesian Estimate Based on Fluorophore Statistics. Biophysj 112:1777–1785.

[32] Zhengxi Huang, Dongmei Ji, S. Wang, , A. Xia, Felix Koberling, M. Patting, , and R. Erdmann, 2005. Spectral Identification of Specific Photophysics of Cy5 by Means of Ensemble and Single Molecule Measurements. The Journal of Physical Chemistry A 110:45–50.

[33] Edwin K L Yeow, Sergey M Melnikov, Toby D M Bell, F. C. D. Schryver, , and J. Hofkens, 2006. Characterizing the Fluorescence Intermittency and Photobleaching Kinetics of Dye Molecules Immobilized on a Glass Surface. The Journal of Physical Chemistry A 110:1726–1734.

[34] Widengren, J., A. Chmyrov, C. Eggeling, P.-Å. Löfdahl, and C. A. M. Seidel, 2007. Strategies to Improve Photostabilities in Ultrasensitive Fluorescence Spectroscopy. The Journal of Physical Chemistry A 111:429–440.

[35] Vogelsang, J., R. Kasper, C. Steinhauer, B. Person, M. Heilemann, M. Sauer, and P. Tinnefeld, 2008. A Reducing and Oxidizing System Minimizes Photobleaching and Blinking of Fluorescent Dyes. Angewandte Chemie International Edition 47:5465–5469.

[36] Veatch, S. L., B. B. Machta, S. A. Shelby, E. N. Chiang, D. A. Holowka, and B. A. Baird, 2012. Correlation Functions Quantify Super-Resolution Images and Estimate Apparent Clustering Due to Over-Counting. PLoS ONE 7:e31457.

[37] Coltharp, C., X. Yang, and J. Xiao, 2014. Quantitative analysis of single-molecule superresolution images. Current opinion in structural biology 28:112–121.

[38] Spahn, C., F. Herrmannsdörfer, T. Kuner, and M. Heilemann, 2016. Temporal accumulation analysis provides simplified artifact-free analysis of membrane-protein nanoclusters. Nature Methods 13:963–964.

[39] Mo, G. C. H., B. Ross, F. Hertel, P. Manna, X. Yang, E. Greenwald, C. Booth, A. M. Plummer, B. Tenner, Z. Chen, Y. Wang, E. J. Kennedy, P. A. Cole, K. G. Fleming, A. Palmer, R. Jimenez, J. Xiao, P. Dedecker, and J. Zhang, 2017. Genetically encoded biosensors for visualizing live-cell biochemical activity at super-resolution. Nature Methods 14:427–434.

[40] Habuchi, S., R. Ando, P. Dedecker, W. Verheijen, H. Mizuno, A. Miyawaki, and J. Hofkens, 2005. Reversible single-molecule photoswitching in the GFP-like fluorescent protein Dronpa. Proceedings of the National Academy of Sciences 102:9511–9516.

[41] Subach, F. V., G. H. Patterson, S. Manley, J. M. Gillette, J. Lippincott-Schwartz, and V. V. Verkhusha, 2009. Photoactivatable mCherry for high-resolution two-color fluorescence microscopy. Nature Methods 6:153–159.

[42] Malagon, F., 2013. RNase III is required for localization to the nucleoid of the 5' pre-rRNA leader and for optimal induction of rRNA synthesis in E. coli. RNA (New York, N.Y.) 19:1200–1207.

[43] Bohrer, C. H., K. Bettridge, and J. Xiao, 2017. Reduction of Confinement Error in Single-Molecule Tracking in Live Bacterial Cells Using SPICER. Biophysical journal 112:568–574.

[44] Das, R., C. W. Cairo, and D. Coombs, 2009. A hidden Markov model for single particle tracks quantifies dynamic interactions between LFA-1 and the actin cytoskeleton. PLoS Computational Biology 5:e1000556.

[45] Zhang, J. and M. S. Shapiro, 2015. Mechanisms and dynamics of AKAP79/150-orchestrated multiprotein signalling complexes in brain and peripheral nerve. The Journal of Physiology 594:31–37.

[46] Zhang, J., C. M. Carver, F. S. Choveau, and M. S. Shapiro, 2016. Clustering and Functional Coupling of Diverse Ion Channels and Signaling Proteins Revealed by Super- resolution STORM Microscopy in Neurons. Neuron 92:461–478.

[47] Cella Zanacchi, F., C. Manzo, R. Magrassi, N. D. Derr, and M. Lakadamyali, 2019. Quantifying Protein Copy Number in Super Resolution Using an Imaging-Invariant Calibration. Biophysj 116:2195–2203.
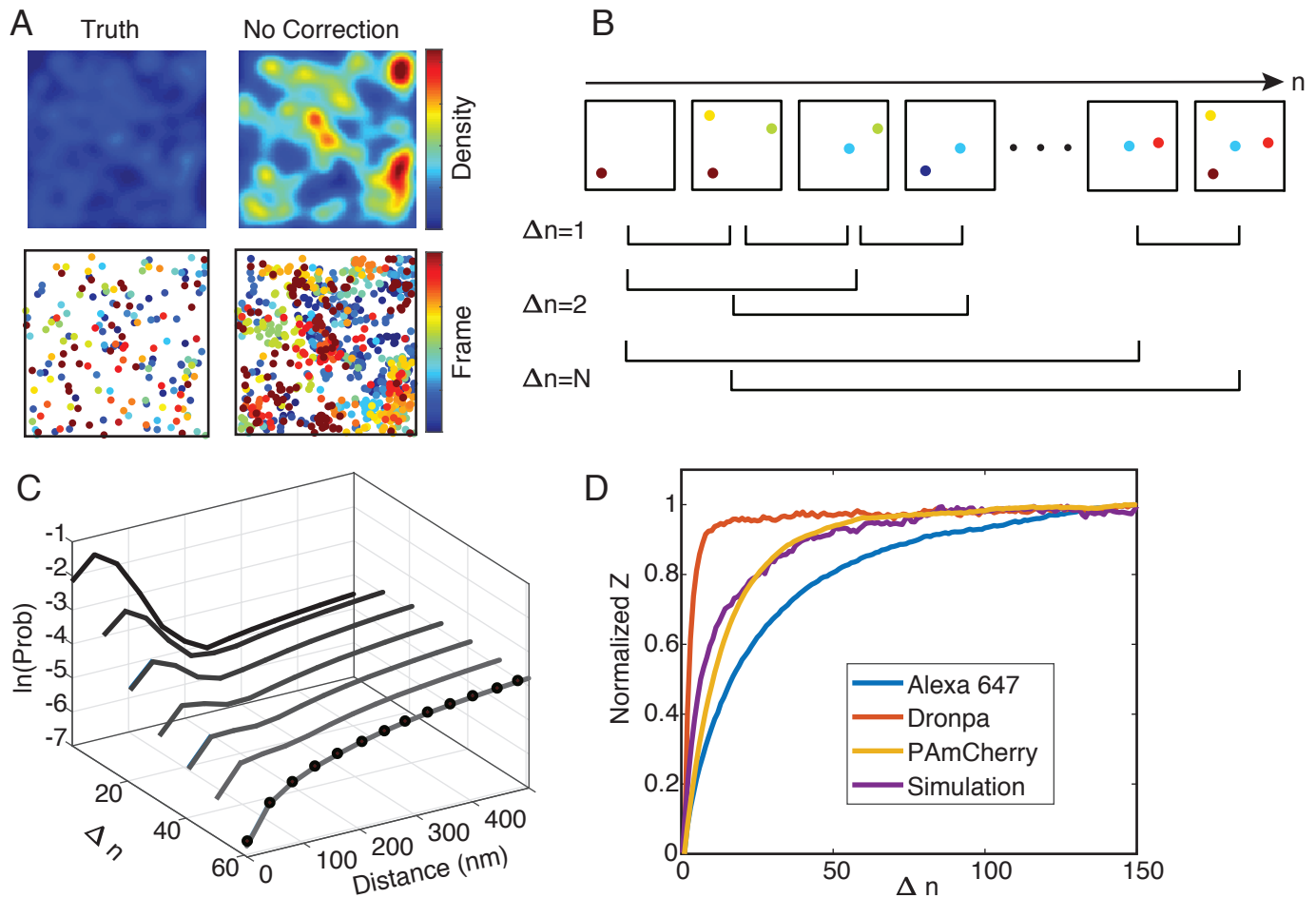
Figure 1: A. Simulated SMLM superresolution images (top panel) of randomly distributed molecules without blinking (Truth) and with blinking (No correction). The corresponding scatter plots (colored through time) are displayed in the bottom panel. B. Schematics of how the pairwise distance distributions at different frame differences (Δn) were calculated. C. Pairwise distance distributions at different Δn (black to gray curves) converge to the true pairwise distribution (black dots) when Δn is large. D. Normalized Z values measured for three commonly used fluorophores and a simulated fluorophore as that used in A. All Z values reach plateaus at large Δn, indicating that at large Δn, the pairwise distance distributions converge to a steady state. The normalized Z value was calculated by taking the difference between the cumulative pairwise distance distribution at a Δn and that at $\Delta n = 1$: ($Z(\Delta n) = \sum |cdf(P_d(\Delta r|\Delta n)) - cdf(P_d(\Delta r|\Delta n = 1))|$).
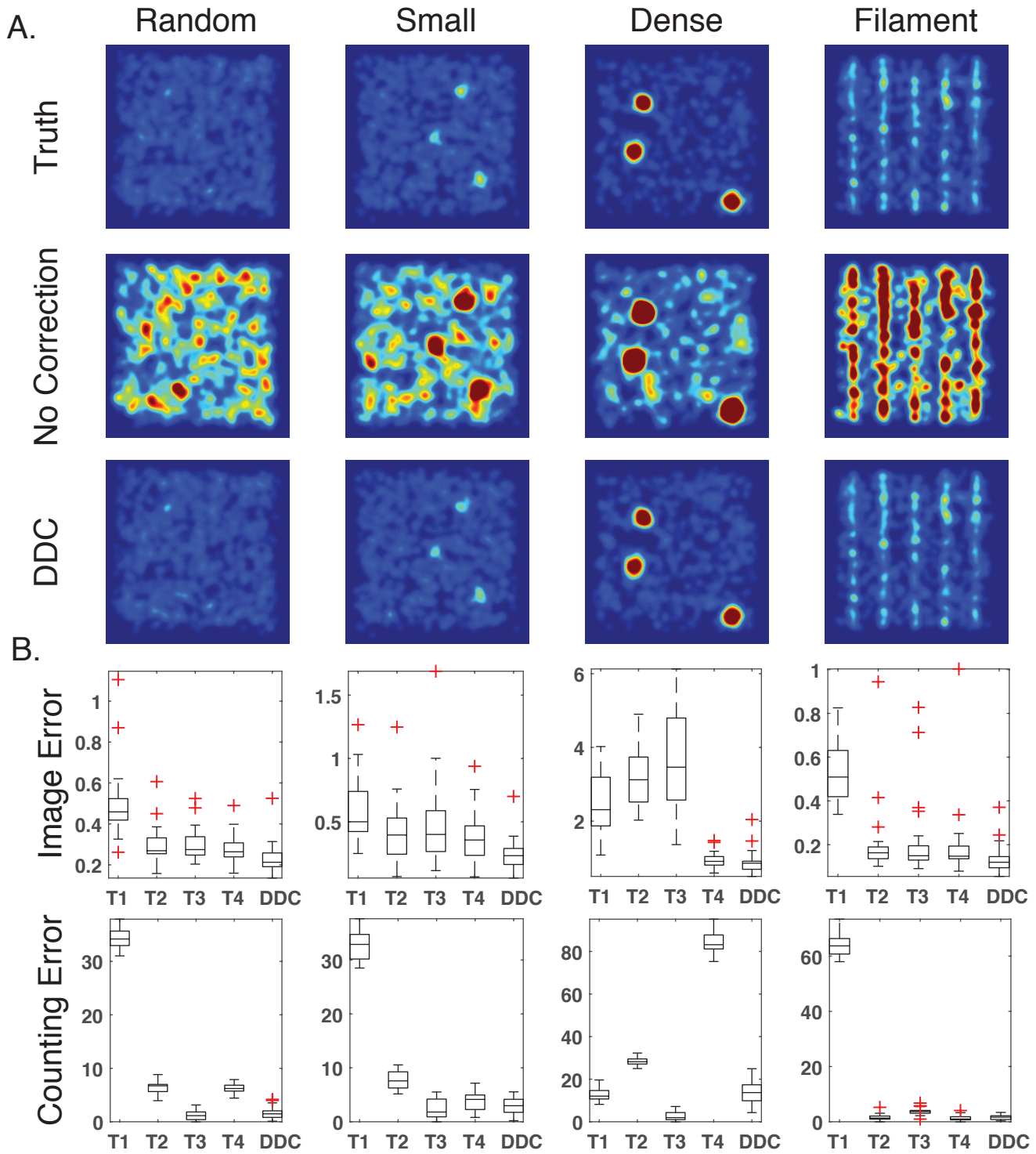
Figure 2: Comparison of four different thresholding methods with DDC on four spatial distributions (randomly distributed, small clusters, dense clusters and filaments). A. True, uncorrected and DDC-corrected images for each spatial distribution. B. Image Error and Counting Error calculated from T1 to T4 and DDC for each spatial distribution. The whiskers extend to the most extreme data points not considered outliers, and the red pluses are the outliers (greater than 2.7 std).
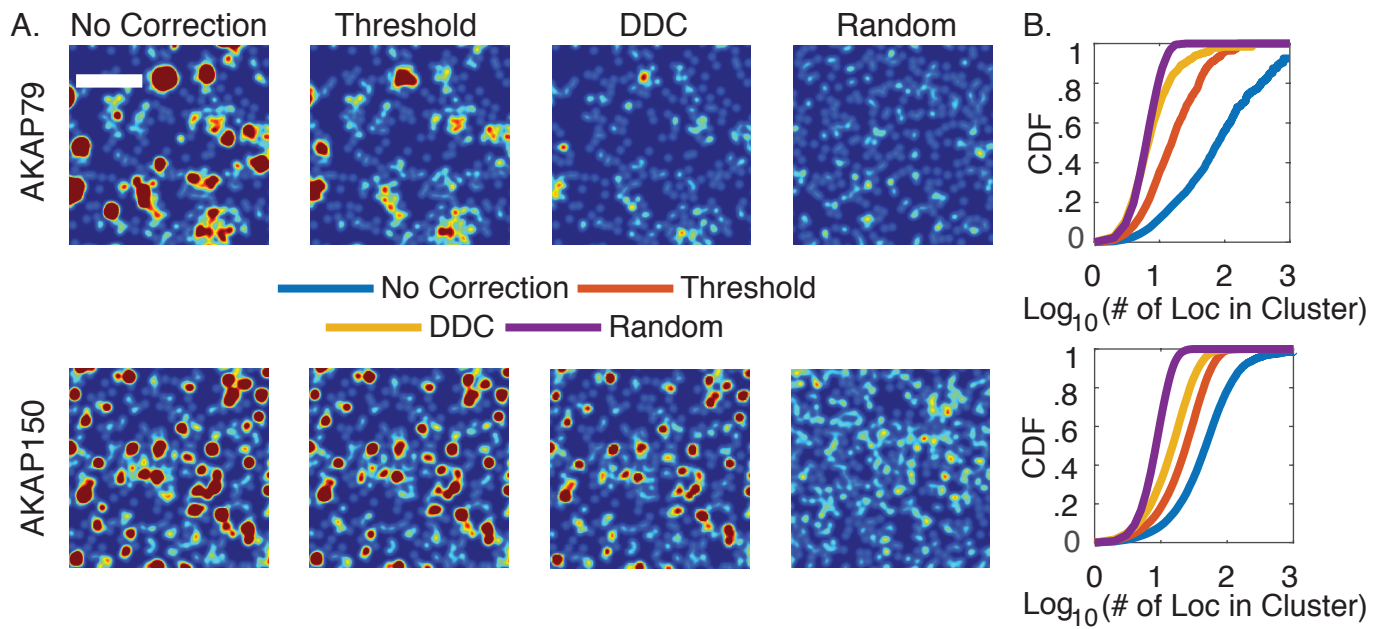
Figure 3: Application of DDC to experimentally measured spatial distributions of AKAP79 and AKAP150. A. SMLM images of the two scaffold proteins without correction, corrected using the thresholding method T1 and DDC, and that of a simulated random distribution using the same number of localizations of DDC-corrected images. B. Cumulative distributions for the number of localizations within each cluster for each protein. (Scale bar, $1\mu m$)
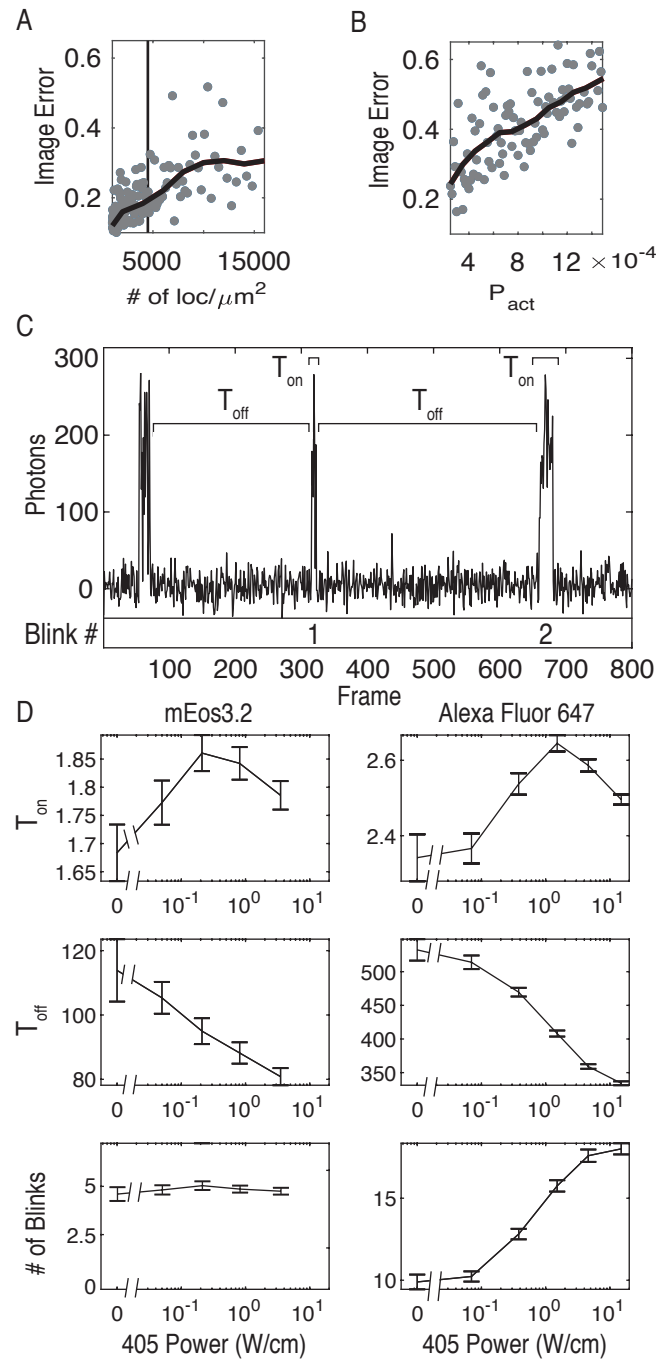
Figure 4: Image Error at different densities of localizations (A) and activation probability per frame (B). The raw data points are shown as gray points and the moving average is shown in black (Supporting Material). C. An intensity trajectory of a single mEos3.2 molecule with labels showing the definitions of T_{on} and T_{off}. D. The average T_{on}, T_{off}, and number of blinks for Alexa647 and mEos3.2 at different UV activation intensities (405 Power, error bars are standard deviation of mean using two repeats).